ARTICLES
https://doi.org/10.1038/s41928-020-00512-6
nature electronics

Reconfigurable photo-induced doping of two-dimensional van der Waals semiconductors using different photon energies

Seung-Young Seo[1,2,5], Gunho Moon[1,2,5], Odongo F. N. Okello[2], Min Yeong Park[1,2], Cheolhee Han[1,2], Soonyoung Cha[1], Hyunyong Choi[3], Han Woong Yeom[1,4], Si-Young Choi[2], Jewook Park[1] and Moon-Ho Jo[1,2,4] ✉

Two-dimensional semiconductors have a range of electronic and optical properties that can be used in the development of advanced electronic devices. However, unlike conventional silicon semiconductors, simple doping methods to monolithically assemble n- and p-type channels on a single two-dimensional semiconductor are lacking, which makes the fabrication of integrated circuitry challenging. Here we report the reversible photo-induced doping of few-layer molybdenum ditelluride and tungsten diselenide, where the channel polarity can be reconfigured from n-type to p-type, and vice versa, with laser light at different frequencies. This reconfigurable doping is attributed to selective light–lattice interactions, such as the formation of tellurium self-interstitial defects under ultraviolet illumination and the incorporation of substitutional oxygen in tellurium and molybdenum vacancies under visible illumination. Using this approach, we create a complementary metal–oxide–semiconductor (CMOS) device on a single channel, where the circuit functions can be dynamically reset from a CMOS inverter to a CMOS switch using pulses of different light frequencies.

Semiconductor doping via the intentional introduction of charged impurities into a semiconductor host lattice—creating either excessive electrons or excessive holes—is the basis of constructing an integrated circuit[1,2]. With monolithic silicon integrated circuits, ion implantation on a single silicon crystal plane is a common doping process[3,4]. However, for two-dimensional (2D) van der Waals (vdW) semiconductor layers, which offer diverse electronic and optical properties[5–14], the construction of monolithic integrated circuits remains challenging because of the absence of a locally selective doping method.

Typically, 2D semiconductors are transition metal dichalcogenides, MX_2, where M is a transition metal and X is a chalcogen atom of sulfur, selenium or tellurium. Compared with elemental semiconductors or oxide semiconductors, the covalent bond strength within the unit monolayers of transition metal dichalcogenides is relatively weak (between 2.3 and 2.9 eV) (ref. [15]), and therefore, their 2D crystals are predisposed to form point defects such as vacancies and self-interstitials[16–20]. These point defects, particularly in the atomically thin host lattices, can be used as donors and acceptors, providing tunability for the carrier types and electrical conductivity[21–23].

In this Article, we report a selective and reversible photo-doping effect in few-layer molybdenum ditelluride (2H-$MoTe_2$) and tungsten diselenide (2H-WSe_2) field-effect transistors (FETs) based on photon-energy-dependent defect generation in the visible (2.33 eV) to ultraviolet (UV; 3.49 eV) radiation regime. We demonstrate precise control over the dopant types and concentrations in a semiconductor channel, and we use our method to construct reconfigurable integrated circuits on monolithic 2D semiconductors. We demonstrate this with a complementary metal–oxide–semiconductor (CMOS) invertor that can be reconfigured into a CMOS switch by reversing the channel polarities with light illumination.

Reconfigurable doping of few-layer $MoTe_2$ and WSe_2 channels

Few-layer 2H-$MoTe_2$ semiconductors, configured in arrays of back-gated FETs on SiO_2/p^+-Si substrates by electron-beam lithography and metal lift-off process, were exposed to two types of continuous-wave laser in air: a visible laser (photon energy, $h\nu = 2.33$ eV, and laser power, $P_{laser} = 20$ mW) and a UV laser ($h\nu = 3.49$ eV and $P_{laser} = 1.5$ mW), as shown in Fig. 1a–d. The laser beam was focused to globally illuminate all the FET channels, where the beam diameter is ~5 μm and the FET channel length and width are typically 1 and 3 μm, respectively (Fig. 1a,b, insets). We define three different 2H-$MoTe_2$ channels within the array, labelled as FET-A, FET-B and FET-C, corresponding to the light illumination sequences. Before any illumination, the pristine channel was characterized as lightly n-type doped, presumably due to native defects and some off-stoichiometry[24].

Under UV illumination at an interval of 10 s, the channel becomes gradually more n-type, as verified in the transfer curve (I_d–V_g) of FET-A, where I_d and V_g are the drain current and applied gate voltage, respectively (Fig. 1a). Then under successive visible illumination, the identical FET-A channel is systematically converted to the p-type (Fig. 1b,e). In turn, when the illumination sequence is reversed on FET-B, the channel type is altered in the same way, that is, the p-type doping with an initial visible illumination, followed by the n-type with UV illumination (Fig. 1c,d,f); this interconversion

[1]Center for Artificial Low Dimensional Electronic Systems, Institute for Basic Science (IBS), Pohang, Korea. [2]Department of Materials Science and Engineering, Pohang University of Science and Technology (POSTECH), Pohang, Korea. [3]Department of Physics and Astronomy, Seoul National University, Seoul, Korea. [4]Department of Physics, Pohang University of Science and Technology (POSTECH), Pohang, Korea. [5]These authors contributed equally: Seung-Young Seo, Gunho Moon. ✉e-mail: mhjo@postech.ac.kr

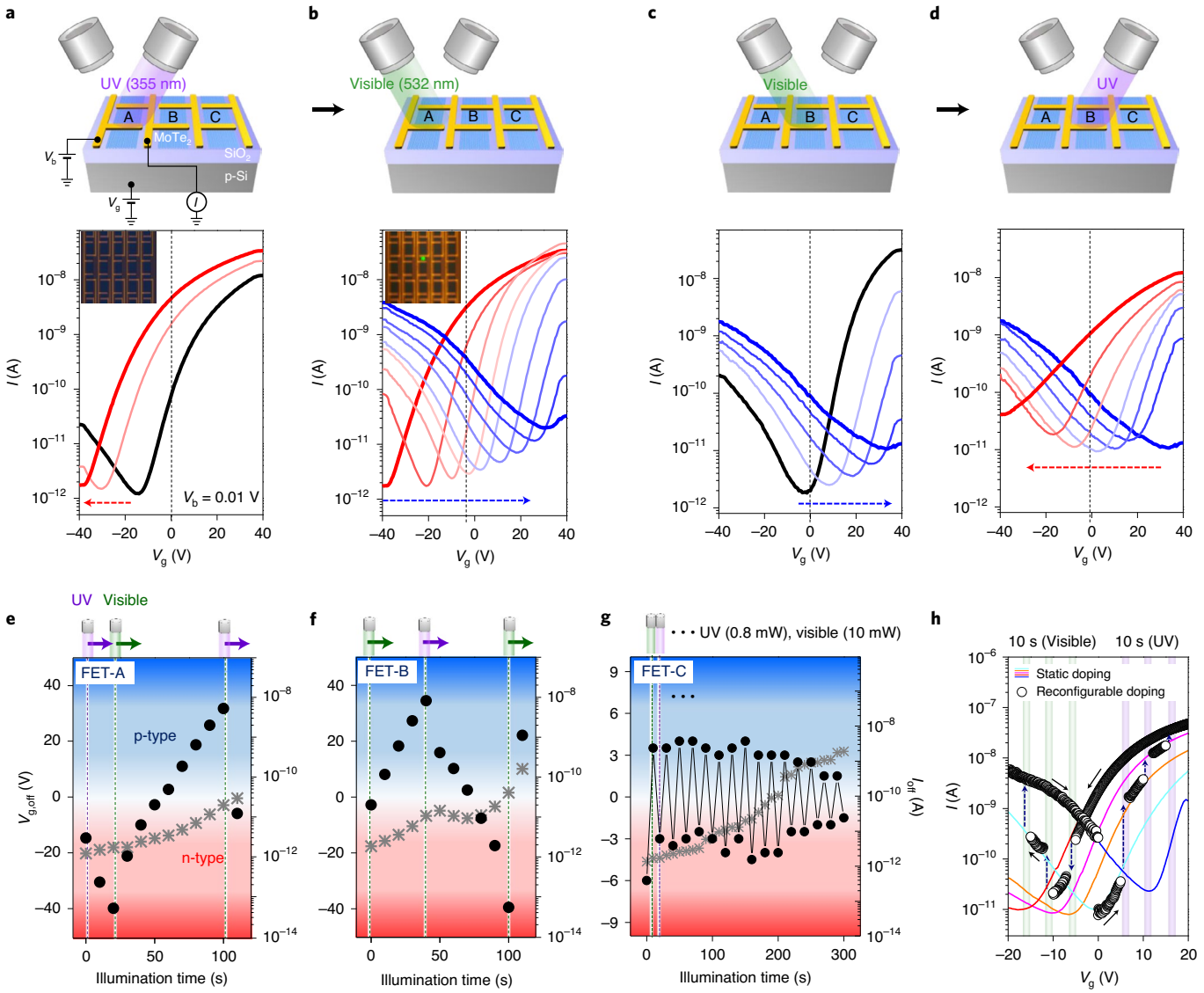

Fig. 1 | Reconfigurable doping on few-layer 2H-$MoTe_2$ channels using different photon energies. a–d, Schematics of the photo-induced doping and transfer characteristics of 2H-$MoTe_2$ back-gated FETs with illumination by a UV laser ($\lambda = 355$ nm, $P_{laser} = 1.5$ mW) (**a**) and subsequently a visible laser ($\lambda = 532$ nm, $P_{laser} = 20$ mW) (**b**) on FET-A, and the visible laser (**c**) and subsequently a UV laser (**d**) on FET-B. Each transfer curve was obtained in 10 s increments of light illumination at a bias voltage (V_b) of 10 mV. The dashed arrows indicate the direction of the shift (n-type doping for red and p-type doping for blue) of transfer curves. Insets in **a** and **b**: optical images during the laser illuminations. **e–g**, Charge-neutral gate voltages ($V_{g,off}$, black circles) and the channel off-current (I_{off}, grey asterisks) upon varying the light sources for FET-A (**e**), FET-B (**f**) and FET-C (**g**). Visible ($\lambda = 532$ nm, $P_{laser} = 10$ mW) and UV ($\lambda = 355$ nm, $P_{laser} = 0.8$ mW) lasers were alternately illuminated on FET-C with the illumination time of 10 s. The background colours indicate the doping state of the channel (n-type for red and p-type for blue). **h**, Transfer characteristics of reconfigurable doping on 2H-$MoTe_2$ FETs. Black circles show the trace of the transfer characteristics during instantaneous doping in the $-20\ V < V_g < 20\ V$ range. The UV laser was illuminated on the 2H-$MoTe_2$ channel at $V_g = 5$, 10 and 15 V and then the visible laser was illuminated at $V_g = -5$, -10 and -15 V. The background colour traces show the transfer characteristics of pristine (cyan) and static doped channels under different doping conditions, namely, 10 s UV (orange), 20 s UV (magenta), 30 s UV (red) and 30 s visible (blue) illumination.

can be repeated over several illumination cycles (FET-C; Fig. 1g). In other words, the channel polarity can be reconfigured with the programmable choice of different coloured light. We summarized such designer doping in Fig. 1e,f by tracing changes in the charge-neutral points ($V_{g,off}$ denotes the V_g at the minimum channel current) in each transfer curve, which systematically swings back and forth between the n- and p-type states according to the light illumination sequences. As shown in Fig. 1g, we have achieved ~30 times the reversible doping cycle under UV (355 nm, 0.8 mW) and visible (532 nm, 10 mW) illumination.

We note that the channel off-current at each charge-neutral point (marked with grey asterisks in Fig. 1e–g) gradually increases as the illumination times are prolonged. This suggests that it is the amount of accumulating defects that determines the maximum number of doping reversals. This also suggests that by tuning the wavelengths and optical powers, the reliability of reversible doping can be further increased. For example, we have achieved ~80 times doping in submicrometre short channels, whose conductance can be precisely tuned in multiple steps under UV (0.8 mW, 1 s) and visible (10 mW, 1 s) illumination conditions (Supplementary Fig. 1).

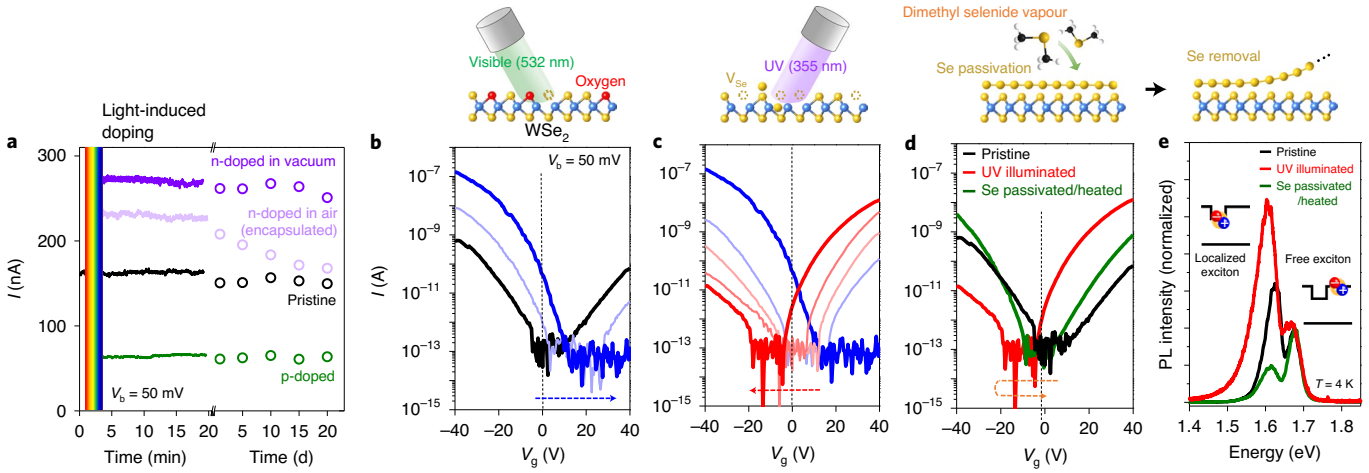

Fig. 2 | Time stability of reconfigurable doping on 2H-$MoTe_2$ and reconfigurable doping on few-layer 2H-WSe_2 channels. a, Conductance traces of pristine $MoTe_2$ channel in air with hBN encapsulation (black), n-doped channel in a vacuum (violet), n-doped channel in air with hBN encapsulation (light violet) and p-doped channel in air with hBN encapsulation (green) measured at a bias voltage of 50 mV. **b**,**c**, Schematics of the selective doping and the corresponding transfer characteristics of 2H-WSe_2 back-gated FETs with illumination by a visible laser ($\lambda = 532$ nm) (**b**) and subsequently by a UV laser ($\lambda = 355$ nm) (**c**). Each transfer curve was obtained after light illumination for 30 s at a bias voltage of 50 mV. The dashed arrows indicate the direction of the shift (n-type doping for red and p-type doping for blue) of transfer curves. **d**, Transfer characteristics of pristine (black), UV-illuminated (red) and Se passivated/heated (green) WSe_2 back-gated FET. The orange dashed arrow indicates the direction of the shift of transfer curves. **e**, Low-temperature (4 K) photoluminescence spectra of pristine (black), UV-illuminated (red) and Se passivated/heated (green) WSe_2 crystal.

In addition, we later discuss a reversible de-doping process on WSe_2 channels by defect healing. In Fig. 1h, we also show 'the dynamically reconfigurable doping scheme', where one can dynamically and reversibly change the specific doping states in less than ~10 s during measurement of the transfer curves: the coloured line traces are from various static photo-doping under fixed light illumination conditions, and the black circle trace denotes instantaneous doping by each light illumination sequence during the I–V_g measurements.

We have recorded the time stability of the doped channels by tracing the channel conductance in time of up to 20 days (Fig. 2a and Supplementary Fig. 2). The doping states are stable under each condition; however, the channel conductance of the n-doped channels decays by a certain degree. We will discuss more on this observation later. This doping can immediately tune the channel resistivity over five orders of magnitude in the time scale of a few tens of seconds, as evident in the temperature-dependent resistivity of various $MoTe_2$ channels doped under different illumination conditions (Supplementary Fig. 3). We also monitored the changes in the FET carrier mobility of both n- and p-doped channels, which initially increases after the first doping (presumably due to the lowered contact barriers by the increasing channel conductance) and slightly decreases over the repeated doping due to the accumulating dopant defects (see the temperature-dependent FET mobility in Supplementary Fig. 4).

The observed doping strategy can be generally applied to other vdW semiconductor channels. We performed similar light-induced doping on few-layer 2H-WSe_2 crystals, which possess a higher bond dissociation energy of ~2.69 eV than that of $MoTe_2$ (2.40 eV)[15]. As shown in Fig. 2b,c, we observed qualitatively the same selective doping: p-type doping with visible illumination (2.33 eV, 20 mW) and n-type doping with UV illumination (3.06 eV, 1.5 mW) in an exchangeable manner. In this case, there is no increase in the channel off-current during the illumination cycles, which is indicative of the higher photochemical stability of 2H-WSe_2. Taking this selective doping a step further, we attempted a reversible de-doping process by eliminating the pre-formed Se vacancy and Se interstitial (V_{Se}/Se_{int}) point defects. For that, the UV-illuminated WSe_2 channels were initially passivated by additional Se layers using dimethyl selenide vapour, which were then removed by thermal heating at 200 °C. At low temperatures (4 K), the photoluminescence spectra of WSe_2 monolayers are known to split into two sub-peaks: free excitonic photoluminescence peak by an interband transition and localized excitonic peak from localized defect states within the bandgap at lower emission energy[25]. After UV illumination, we observed that the localized excitonic peak intensity substantially increases (Fig. 2e, red curve); subsequently, upon Se passivation/removal, it reversibly decreased (Fig. 2e, green curve). This result confirms that the pre-formed defects can be healed with Se passivation, thus enabling the de-doping process. We verified that the transfer curve recovered to the pristine channel state under Se passivation/removal from the UV-induced n-type doping strategy.

Doping polarity versus light frequency and intensity

To more closely investigate the doping selectivity of 2H-$MoTe_2$ channels, we recorded the changes in the transfer curves (Fig. 3) by varying the monochromatic light energy (2.33–3.06 eV) and light power (0.1–20 mW); an extended version of the doping diagram is shown in Supplementary Fig. 5. The principal observations can be summarized as follows. First, at 2.33 eV illumination, the p-type doping is more pronounced at a higher optical intensity. Second, at a constant optical power of 1.5 mW, the channel polarity starts to shift to the n-type direction, when $h\nu$ increases from 2.33 to 2.58 eV, and becomes the more distinct n-type in a higher photon energy range. Third, at 3.06 eV illumination, n-type doping is much more noticeable up to almost degenerate levels at a higher intensity of up to 20 mW. It is interesting to note that the transition from the p-type to n-type doping occurs within $2.33 < h\nu < 2.58$ eV, which is just below and above the bond dissociation energy of 2.40 eV, respectively[15], as shown in Fig. 3, inset. This suggests that our observations on photo-selective doping can be discussed within the framework of light–lattice interactions. Upon optical absorption across the energy bandgap of ~1 eV in 2H-$MoTe_2$ (ref. [26]), the absorbed light delivers the characteristic photon energy to the host lattices. When $h\nu$ is comparable or greater than the bond dissociation energy of ~2.40 eV, it can induce photochemical decompositions, that is, the creation of vacancies and interstitial atoms in the host lattices.

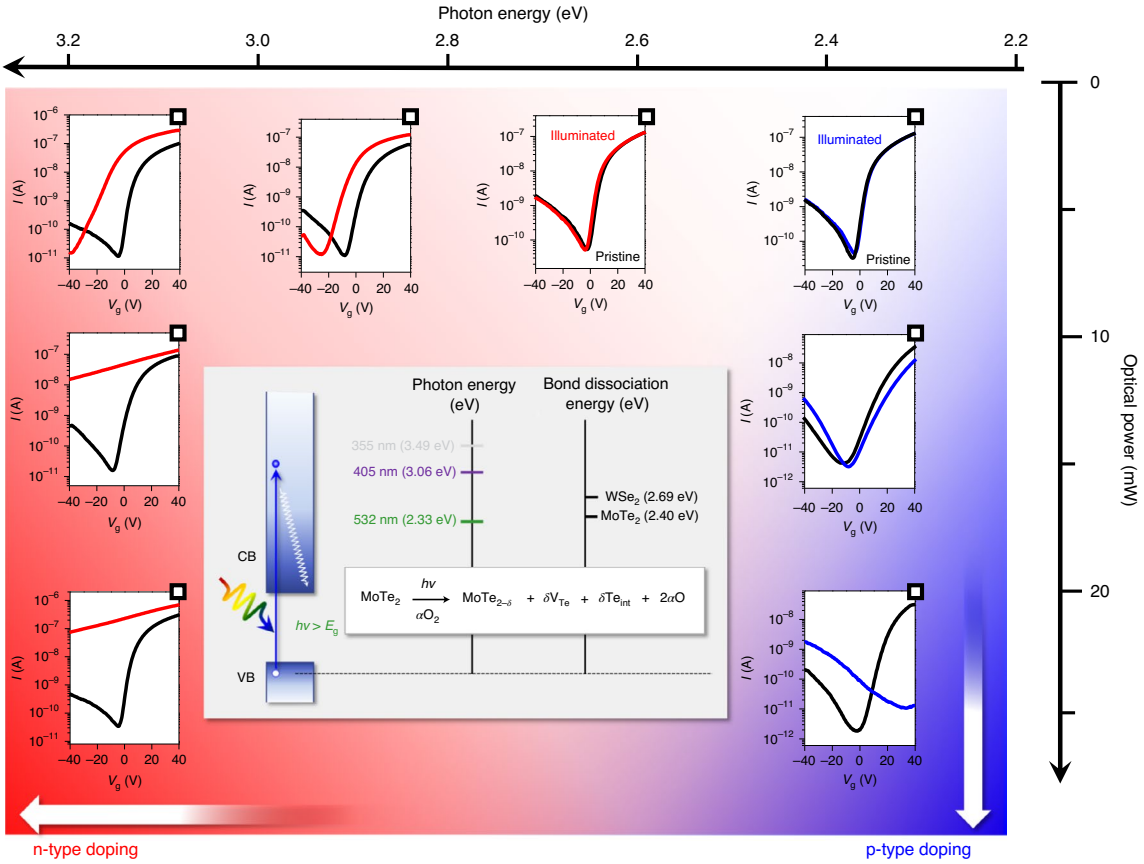

Fig. 3 | Doping polarity versus light frequency and intensity. FET transfer characteristics of the 2H-$MoTe_2$ channel before (black) and after (coloured) light illumination at different photon energies and optical powers. Black squares on the top right corner of each plot indicate the different light illumination conditions. The inset shows a schematic of the energy band diagram of 2H-$MoTe_2$ upon photoexcitation, bond dissociation energy of 2H-$MoTe_2$ and 2H-WSe_2, and the photochemical reaction equation for this work. VB, valence band; CB, conduction band.

Light absorption also provides heat to the lattices, which is proportional to the light intensity. For example, we estimate that the equilibrium temperature can go up to ~477 °C at an optical power of 20 mW under 532 nm laser illumination. Consequently, near *hv* of ~2.40 eV, the photon energy primarily decides whether the photochemical decompositions occur and the optical power defines the local temperature at such reactions. Then the types and number of point defects can be determined by two similar variables under a given illumination condition. In the following section, we verify such light–lattice interactions on selective doping by atomic-scale defect observations obtained using scanning transmission electron microscopy (STEM), scanning tunnelling microscopy (STM) and scanning tunnelling spectroscopy (STS).

Atomic-scale observations of individual dopants

Figure 4a,b shows the in-plane lattice images after UV and visible illumination, taken by a high-angle annular dark-field (HAADF)–STEM instrument, where the representative types of point defect in the hexagonal host lattices are marked with different coloured arrows. Here we have taken images from the 2H-$MoTe_2$ bilayers to highlight the clearer atomic contrast of the individual defects. After UV illumination (Fig. 4a and Supplementary Fig. 6), the most prominent defects were identified as Te vacancies (V_{Te}, red arrows) and Te self-interstitials (Te_{int}, blue and green arrows) with a smaller portion of Mo vacancies (V_{Mo}). Specifically, V_{Te} mostly comprised single or double vacancies and the lateral positions of Te_{int} were either right on the Te of the $MoTe_2$ lattice or within the Mo–Te hexagonal hollows (Fig. 4a, bottom); here such additional Te atoms are termed as 'Te interstitials (Te_{int})' regardless of the specific interstices. On the other hand, under visible illumination (Fig. 4b), the defects were predominantly Te vacancies filled with another light element, and therefore a substitutional light atom, with a smaller portion of V_{Te} and V_{Mo}. The HAADF and annular bright-field (ABF) STEM images, as well as the corresponding line profiles (Fig. 4b, bottom), show the contrast between V_{Te} and the light-element-filled V_{Te} in the host lattice (Supplementary Fig. 7). We assigned such light elements to oxygen (O), as we detected notable O content from the cross-sectional energy-dispersive X-ray spectroscopy from the TEM specimen under investigation (Supplementary Fig. 8), which is similar to our earlier work[27]. This assignment is also consistent with recent reports on O-substitutional defects as the most stable species, directly probed by low-temperature atomic force microscopy in conjunction with theoretical calculations[25,28–33]. Indeed, from our atmosphere-controlled FET experiments, we have observed a strong p-type channel conversion exclusively in air and O_2 gas under visible illumination; under either a vacuum or N_2 gas, we observed the opposite n-type conversion (Supplementary Fig. 9). We termed these oxygen-filled V_i as 'V_i–O pairs' (i = Te or Mo). Therefore, the distinctive defects that pertain to each light colour were identified: Te_{int} for UV illumination and V_i–O pairs for visible illumination. Further, V_{Te} and V_{Mo} were commonly found regardless of the light colours.

We then investigated the local electronic structures near such characteristic defect sites by using STM/STS, performed on in situ

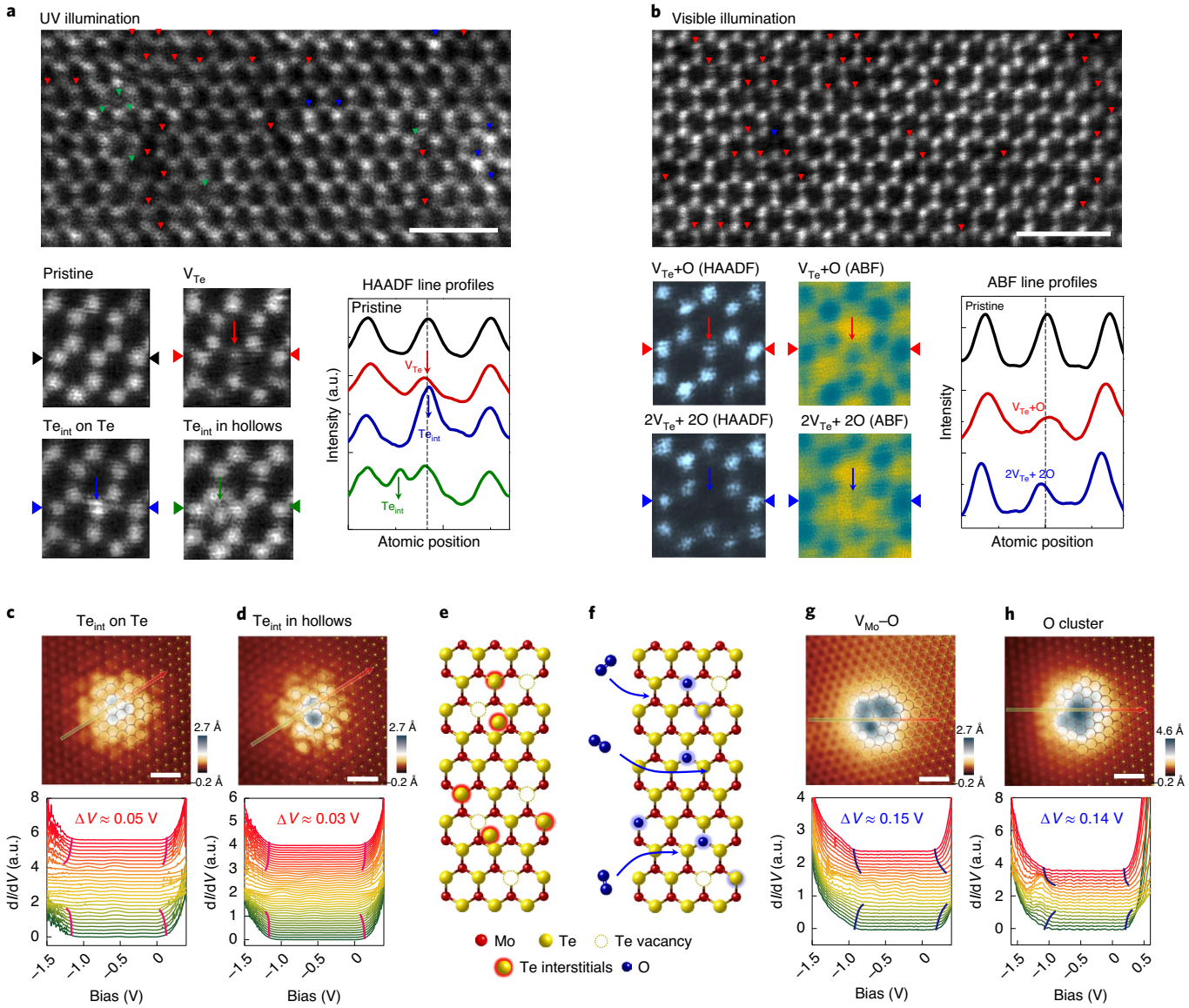

Fig. 4 | Atomic-scale observations of individual dopants. a,**b**, STEM images of UV-light-illuminated (**a**) and visible-light-illuminated (**b**) 2H-$MoTe_2$ crystals, where the representative point defects are marked with different coloured arrows. In the bottom images, each type of point defect is shown in the enlarged images along with the TEM intensity line profiles along the marked direction. **c**,**d**, STM images and variation in the d*I*/d*V* line spectra by STS near the characteristic point defects such as Te_{int} at the Te site (**c**) and Te_{int} at the hollow site (**d**). **e**,**f**, Schematic in-plane crystal structures including point defects of UV-light-illuminated (**e**) and visible-light-illuminated (**f**) 2H-$MoTe_2$ crystals. **g**,**h**, STM images and variation in the d*I*/d*V* line spectra near a V_{Mo}–O pair (**g**) and an O cluster (**h**). Colour arrows in **c**, **d**, **g** and **f** indicate the direction of STM tip position changes, which are correlated to the colours of the d*I*/d*V* curves in each bottom graph. Scale bars (STEM images in **a** and **b** and STM images in **c**, **d**, **g**, and **h**), 1 nm.

cleaved 2H-$MoTe_2$ surfaces in an ultrahigh vacuum after each light illumination (Supplementary Fig. 10); here note that we employed thicker crystals (~30–50 layers) to reproducibly obtain the cleaved surfaces, which were originally imbedded within the bulk vdW gaps. The STM topography images of the defects (Fig. 4c,d) and the differential conductance(d*I*/d*V*) line spectra, which are proportional to the local density of states (LDOS), largely confirm the similar defect types defined by STEM. For example, upon UV illumination, Te_{int} was consistently observed on the Te lattice atoms or within the hollows (Supplementary Fig. 11) for the large-area scanned images. The LDOS near such Te_{int} (Fig. 4c,d, bottom) show that the LDOS substantially shifts by ~30–50 meV towards the occupied states. This local band bending implies that Te_{int} acts as an electron donor to the neighbouring lattices, while we have detected little variation in the LDOS at the V_{Te}. The electron-donating characteristic of Te_{int} is directly consistent with the n-type FET conversion under UV illumination (Fig. 1). Meanwhile, after visible illumination, we observed additional O-paired species, such as V_{Mo}–O pairs or O clusters (Fig. 4g,h). These O clusters are stable over repeated tip scanning, implying that they are bonded to the host lattices, presumably to either V_{Te} or V_{Mo}, although the atomic positions cannot be resolved due to the cluster size. For both the O-paired species, we commonly observed a strong LDOS shift towards the unoccupied states by 140–150 meV with clear mid-gap states near the valence band maximum, which is also consistent with recent observations of substitutional O resonant states near the valence band maximum in $MoSe_2$ and WS_2 (ref. [28]).

The band bending in our case showed a substantial spatial extent of over 1 nm (Fig. 4g,h, bottom). The signal decay length is shown

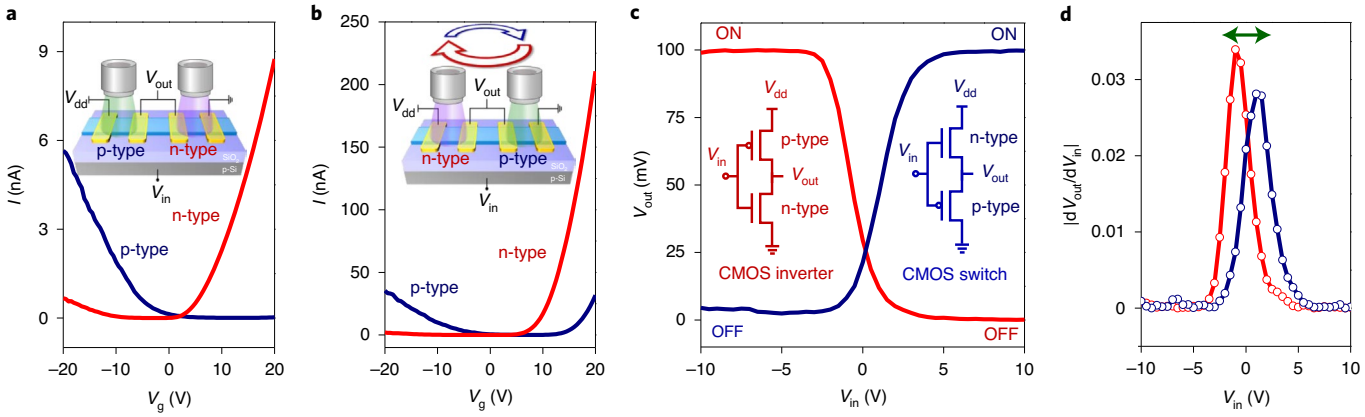

Fig. 5 | Reconfigurable CMOS inverter–switch tuned at different light frequencies. a,**b**, FET transfer characteristics of a pair of 2H-$MoTe_2$ channels with opposite carrier types to form a CMOS circuit. Initially, the left (right) channel is a p-type (n-type) channel under visible (UV) illumination; subsequently, the channel polarities are reversed under opposite light illumination, that is, the left (right) channel converts to an n-type (p-type) channel under UV (visible) illumination. **c**, Voltage transfer characteristics of the CMOS inverter from the configuration of **a** (red) and the CMOS switch of **b** (blue). **d**, Gain characteristics of the CMOS inverter (red) and CMOS switch (blue) tuned at different light-colour combinations. The green arrow indicates the shift of maximum gain.

in Supplementary Fig. 12. This signifies that these O-paired defects are shallow-level electron acceptors, responsible for the p-type conversion (Fig. 1). These features of shallow-doping-level states are consistent with the shift in the photocurrent onset edges at low temperatures (4 K) (Supplementary Fig. 13) and the local band-bending directions at the metal contacts, as verified by the photocurrent mapping (Supplementary Fig. 14).

Based on the STEM and STM/STS results, the net photochemical reaction (Fig. 3, middle) can be expressed as

$$\mathrm{MoTe_2} \xrightarrow[\alpha \mathrm{O_2}]{h\nu} \mathrm{MoTe_{2-\delta}} + \delta \mathrm{V_{Te}} + \delta \mathrm{Te_{int}} + 2\alpha \mathrm{O}, \qquad (1)$$

where the α and δ indicate the arbitrary small numbers. Then we summarize our selective doping processes as follows: the photo-induced Te_{int} formation, which is mainly responsible for the n-type conversion as an electron donor, is substantially dominant when $h\nu > 2.40$ eV. At $h\nu < 2.40$ eV, substantial heat—provided by the large enough optical power—efficiently incorporates oxygen from the atmosphere into either the V_{Te} or V_{Mo} sites to form V_i–O pairs (i = Te or Mo), which, in turn, act as electron acceptors for p-type conversion. That is, Te_{int} formation and V_i–O pair formation are two competing processes at a given photon energy and light intensity. In our work, the n-type conversion is stabilized under UV illumination ($h\nu > 2.40$ eV) at a smaller optical power (1.5 mW) and p-type conversion is facilitated under visible illumination ($h\nu < 2.40$ eV) at a larger optical power (up to 20 mW).

Reconfigurable CMOS inverter–switch

Our light-colour selective doping on 2D semiconductors allows us to demonstrate a proof-of-concept device, where the circuit functions are reconfigurable. Figure 5a shows a CMOS inverter in which the left and right channels are indicated as p-type and n-type channels with visible- and UV-light illumination, respectively, as verified by the corresponding back-gate voltage transfer characteristics. The red curve in Fig. 5c shows a CMOS inverter, where the output voltage (V_{out}) is zero for a positive input voltage (V_{in}), and V_{out} is equal to supply voltage (V_{dd}) at a negative V_{in}. Then, by interchanging the light colours, we interconverted the polarity of each channel, as shown in Fig. 5b, to form a CMOS switch, where the V_{out}–V_{in} relationship is opposite to the inverter (blue curve in Fig. 5c). That is, with the choice of light colours, the circuit can be reconfigured from a CMOS inverter to a CMOS switch, and vice versa (Fig. 5d).

Conclusions

We have reported a reconfigurable doping method for 2D vdW semiconductors that is based on selective light–lattice interactions for different photon energies. The control of the carrier type and doping levels in few-layer $MoTe_2$ and WSe_2 FETs was demonstrated and used to fabricate reconfigurable CMOS integrated circuits. In addition, we provide visual and spectroscopic evidences of individual n- and p-type dopants, which dynamically interact with the light. The working principles of our photo-doping method could be used to develop monolithic integrated circuits on 2D semiconductors, similar to ion implantation in silicon CMOS technology. Point defects as dopants in the host semiconductor lattice, such as vacancies and interstitials, can often be less stable than substitutional dopants with foreign atoms, which form stronger chemical bonds in the lattice, and are thus subject to additional interactions (such as diffusion and oxidation). While the p-type channel in our work remains stable under air exposure for over a month, the polarity of the n-type channel tends to persist in air when encapsulated by hexagonal boron nitride (hBN) layers (Supplementary Fig. 15). Our work on photo-induced doping may call for further investigations into substitutional doping, such as substitutional n- and p-dopant atoms with stronger bonding strength.

Methods

Device fabrication. Our 2H-$MoTe_2$ crystals were mechanically exfoliated from a commercially available crystal (2D semiconductors labelled with purity of 99.9999% and a defect concentration of ~10^{12} cm^{-2}). We fabricated back-gated 2H-$MoTe_2$ FETs on SiO_2 (300 nm or 100 nm)/p^+Si substrates using electron-beam lithography and electron-beam evaporation for electrodes (Ti 1 nm/Au 40 nm).

Photo-induced doping of 2D vdW semiconductors. The incident laser beam was illuminated on the 2D vdW semiconductor channels under global illumination conditions, where the beam diameter is ~5 μm. We tuned the global illumination condition by setting the z-axis offset (~2 μm) in the piezocontroller of a home-built confocal microscope system.

TEM analyses of bilayer 2H-$MoTe_2$. Mechanical exfoliation method was used to prepare a bilayer 2H-$MoTe_2$ specimen on 200 mesh gold quantifoils using a blue Scotch tape and a poly methyl methacrylate (PMMA) stamp. TEM analyses were carried out using a JEOL ARM200F instrument equipped with a fifth-order

spherical aberration (C_s) corrector (ASCOR/CEOS). The acceleration voltage of 80 kV was chosen to minimize electron-beam damage to the specimen. The camera length was chosen as 5 cm for ABF imaging under 80 kV. The image simulations were conducted using Dr. Probe (Ernst Ruska-Centre for Microscopy and Spectroscopy with Electrons, version 1.8), an open-source simulation software.

STM/STS analyses on individual dopants of 2H-$MoTe_2$. STM/STS measurements were performed using low-temperature STM (Unisoku) and Nanonis (SPECS) instruments. Light-illuminated 2H-$MoTe_2$ layers are prepared under ambient conditions similar to the fabrication of the FETs; then, they were transferred into an ultrahigh vacuum ($<1\times10^{-10}$ torr) STM chamber. Most of the top layers were delaminated by in situ cleavage under the ultrahigh vacuum condition at room temperature[27]. We employed electrochemically etched tungsten tips, and we used the lock-in technique with 500 Hz, 10–50 mV a.c. modulations. All the STM/STS measurements were performed at 78 K, and the data were analysed with both WSxM and Gwyddion software.

Data availability

The data that support the plots within this paper and other findings of this study are available from the corresponding author upon reasonable request.

Received: 26 January 2020; Accepted: 12 November 2020;
Published online: 14 December 2020

References

1. Queisser, H. J. & Haller, E. E. Defects in semiconductors: some fatal, some vital. *Science* **281**, 945–950 (1998).
2. Norris, D. J., Efros, A. L. & Erwin, S. C. Doped nanocrystals. *Science* **319**, 1776–1779 (2008).
3. Ohl, R. S. Properties of ionic bombarded silicon. *Bell Syst. Tech. J.* **31**, 104–121 (1952).
4. Mak, K. F., Lee, C., Hone, J., Shan, J. & Heinz, T. F. Atomically thin MoS_2: a new direct-gap semiconductor. *Phys. Rev. Lett.* **105**, 136805 (2010).
5. Lee, C.-H. et al. Atomically thin p–n junctions with van der Waals heterointerfaces. *Nat. Nanotechnol.* **9**, 676–681 (2014).
6. Heo, H. et al. Interlayer orientation-dependent light absorption and emission in monolayer semiconductor stacks. *Nat. Commun.* **6**, 7372 (2015).
7. Srivastava, A. et al. Optically active quantum dots in monolayer WSe_2. *Nat. Nanotechnol.* **10**, 491–496 (2015).
8. Huang, B. et al. Layer-dependent ferromagnetism in a van der Waals crystal down to the monolayer limit. *Nature* **546**, 270–273 (2017).
9. Kim, J. et al. Ultrafast generation of pseudo-magnetic field for valley excitons in WSe_2 monolayers. *Science* **346**, 1205–1208 (2014).
10. Cui, X. Multi-terminal transport measurements of MoS_2 using a van der Waals heterostucture device platform. *Nat. Nanotechnol.* **10**, 534–540 (2015).
11. Desai, S. B. et al. MoS_2 transistors with 1-nanometer gate lengths. *Science* **354**, 99–102 (2016).
12. Kang, K. et al. Layer-by-layer assembly of two-dimensional materials into wafer-scale heterostructures. *Nature* **550**, 229–233 (2017).
13. Jauregui, L. A. et al. Electrical control of interlayer exciton dynamics in atomically thin heterostructures. *Science* **366**, 870–875 (2019).
14. Seyler, K. L. et al. Signatures of moiré-trapped valley excitons in $MoSe_2$/WSe_2 heterobilayers. *Nature* **567**, 66–70 (2019).
15. Liu, H., Han, N. & Zhao, J. Atomistic insight into the oxidation of monolayer transition metal dichalcogenides: from structures to electronic properties. *RSC Adv.* **5**, 17572–17581 (2015).
16. Komsa, H.-P. et al. Two-dimensional transition metal dichalcogenides under electron irradiation: defect production and doping. *Phys. Rev. Lett.* **109**, 035503 (2012).
17. Komsa, H.-P. & Krasheninnikov, A. V. Native defects in bulk and monolayer MoS_2 from first principles. *Phys. Rev. B* **91**, 125304 (2015).
18. Zou, X. & Yakobson, B. I. An open canvas—2D materials with defects, disorder, and functionality. *Acc. Chem. Res.* **48**, 73–80 (2015).
19. Haldar, S., Vovusha, H., Yadav, M. K., Eriksson, O. & Sanyal, B. Systematic study of structural, electronic, and optical properties of atomic-scale defects in the two-dimensional transition metal dichalcogenides MX_2 (M = Mo, W; X = Se, Te). *Phys. Rev. B* **92**, 235408 (2015).
20. Rhodes, D., Chae, S. H., Ribeiro-Palau, R. & Hone, J. Disorder in van der Waals heterostructures of 2D materials. *Nat. Mater.* **18**, 541–549 (2019).
21. Wu, E. et al. Dynamically controllable polarity modulation of $MoTe_2$ field-effect transistors through ultraviolet light and electrostatic activation. *Sci. Adv.* **5**, eaav3430 (2019).
22. Liu, T. et al. Nonvolatile and programmable photodoping in $MoTe_2$ for photoresist-free complementary electronic devices. *Adv. Mater.* **30**, 1804470 (2018).
23. Wu, G. et al. Programmable transition metal dichalcogenide homojunctions controlled by nonvolatile ferroelectric domains. *Nat. Electron.* **3**, 43–50 (2020).
24. Conan, A., Goureaux, G. & Zoaeter, M. Transport properties of $MoTe_{2-x}$ and $MoSe_{2-x}$ compounds between 130 and 300°K. *J. Phys. Chem. Solids* **36**, 315–320 (1975).
25. Zhang, S. et al. Defect structure of localized excitons in a WSe_2 monolayer. *Phys. Rev. Lett.* **119**, 046101 (2017).
26. Ruppert, C., Aslan, O. B. & Heinz, T. F. Optical properties and band gap of single- and few-layer $MoTe_2$ crystals. *Nano Lett.* **14**, 6231–6236 (2014).
27. Seo, S.-Y. et al. Writing monolithic integrated circuits on a two-dimensional semiconductor with a scanning light probe. *Nat. Electron.* **1**, 512–517 (2018).
28. Chen, B. et al. Environmental changes in $MoTe_2$ excitonic dynamics by defects-activated molecular interaction. *ACS Nano* **9**, 5326–5332 (2015).
29. Qu, D. et al. Carrier-type modulation and mobility improvement of thin $MoTe_2$. *Adv. Mater.* **29**, 1606433 (2017).
30. Park, J. H. et al. Defect passivation of transition metal dichalcogenides via a charge transfer van der Waals interface. *Sci. Adv.* **3**, e1701661 (2017).
31. Barja, S. et al. Identifying substitutional oxygen as a prolific point defect in monolayer transition metal dichalcogenides. *Nat. Commun.* **10**, 3382 (2019).
32. Liu, Y., Stradins, P. & Wei, S.-H. Air passivation of chalcogen vacancies in two-dimensional semiconductors. *Angew. Chem. Int. Ed.* **55**, 965–968 (2016).
33. Lu, J. et al. Atomic healing of defects in transition metal dichalcogenides. *Nano Lett.* **15**, 3524–3532 (2015).

Acknowledgements

This work was supported by the Institute for Basic Science (IBS), Korea, under project code IBS-R014-A1.

Author contributions

S.-Y.S., G.M. and M.-H.J. conceived and designed the project. S.-Y.S., G.M., C.H., S.C. and H.C. conducted the device fabrication, photo-induced doping and electrical measurements. O.F.N.O. and S.-Y.C. performed the TEM measurements and analysed the data. J.P. and H.W.Y. performed the STM measurements and analysed the data. M.Y.P. performed the metal–organic chemical vapour deposition growth of the WSe_2 channels. S.-Y.S., G.M. and M.-H.J. wrote the paper. All the authors discussed the results and commented on the manuscript.

Competing interests

The authors declare no competing interests.

Additional information

Supplementary information is available for this paper at https://doi.org/10.1038/s41928-020-00512-6.

Correspondence and requests for materials should be addressed to M.-H.J.

Reprints and permissions information is available at www.nature.com/reprints.

Publisher's note Springer Nature remains neutral with regard to jurisdictional claims in published maps and institutional affiliations.